

# Observation of unconventional spin polarization induced spin orbit torque in L1<sub>2</sub>-ordered antiferromagnetic Mn<sub>3</sub>Pt thin films

Longjie Yu,<sup>1, a)</sup> Shutaro Karube,<sup>2, 3</sup> Min Liu,<sup>1</sup> Masakiyo Tsunoda,<sup>3, 4</sup> Mikihiro Oogane,<sup>1, 3, 5</sup> and Yasuo Ando<sup>1, 3, 5</sup>

<sup>1)</sup>Department of Applied Physics, Tohoku University, Sendai 980-8579, Japan

<sup>2)</sup>Department of Materials Science, Tohoku University, Sendai 980-8579, Japan

<sup>3)</sup>Center for Spintronics Research Network, Sendai 980-8579, Japan

<sup>4)</sup>Department of Electronic Engineering, Tohoku University, Sendai 980-8579, Japan

<sup>5)</sup>Center for Science and Innovation in Spintronics, Sendai 980-8579, Japan

(Dated: 22 September 2021)

Non-collinear antiferromagnets exhibits richer magneto-transport properties due to the topologically nontrivial spin structure they possess compared to conventional nonmagnetic materials, which allows us to manipulate the charge-spin conversion more freely by taking advantage of the chirality. In this work, we explore the unconventional spin orbit torque of L1<sub>2</sub>-ordered Mn<sub>3</sub>Pt with a triangular spin structure. We observed an unconventional spin orbit torque along the  $\mathbf{x}$ -direction for the (001)-oriented L1<sub>2</sub> Mn<sub>3</sub>Pt, and found that it has a unique sign reversal behavior relative to the crystalline orientation. This generation of unconventional spin orbit torque for L1<sub>2</sub>-ordered Mn<sub>3</sub>Pt can be interpreted as stemming from the magnetic spin Hall effect. This report help clarify the correlation between the topologically nontrivial spin structure and charge-spin conversion in non-collinear antiferromagnets.

Many newly discovered phenomena associated with the topology of magnetism make antiferromagnets (AFMs) with topologically nontrivial spin structures a rich playground for the investigation of unique topological behaviors, as well as promising candidates for energy-efficient microelectronic applications<sup>1-3</sup>. The anomalous transport properties of electrons and magnons that are affected by spin structure induced non-vanishing Berry curvatures<sup>4,5</sup> or chirality-related Dzyaloshinskii-Moriya interaction<sup>6</sup>, known as the anomalous Hall effect (AHE) and magnetic skyrmions respectively, make it possible to control the charge or magnon transport in AFMs efficiently and stably. AFMs have also attracted interest because it is possible to not only use them as efficient spin current sources<sup>7-9</sup> but also to modulate their spin structures electrically<sup>10-12</sup>, which leads to great application potential. More recently, the discovery of magnetic spin Hall effect (MSHE)<sup>13-15</sup> in non-collinear AFMs with topological triangular spin structures and the observation of Berry curvature-induced spin-orbit torque (SOT)<sup>16,17</sup> in collinear AFM with a parallel spin structure have been highlighted, both of which provide the opportunity to manipulate the spin current and generate spin polarization by tuning the spin structures of AFMs.

Although the charge-to-spin conversion phenomenon of MSHE is similar to that of the intrinsic conventional spin Hall effect (SHE), the time-reversal symmetry of MSHE is odd and of extrinsic origin, which makes it a reactive counterpart of SHE and demonstrative of a dissipative nature<sup>13-15,18</sup>. The odd time-reversal symmetry can be regarded as the result of magnetic-order parameter reversal, which indicates that the spin polarization  $\sigma$  generated by MSHE is dictated by the magnetic order, thereby

allowing an in-plane component in the form of scattering plane created by the charge current and spin current. In other words, in current-induced SOT, MSHE is expected to generate an additional NO- $\mathbf{y}$  spin polarization, *i.e.*,  $\mathbf{x}$ -polarization and  $\mathbf{z}$ -polarization when the charge current is flowing along the in-plane direction ( $\mathbf{x}$  direction), whereas only  $\mathbf{y}$ -polarization is allowed to exist for SHE due to the restriction of symmetry<sup>13,16,19</sup>. Analogous to the  $\mathbf{y}$ -polarization which generated by SHE will give rise to a conventional damping-like (DL) torque in an adjacent ferromagnet (FM) of the form  $\mathbf{m} \times (\mathbf{m} \times \mathbf{y})$ , where  $\mathbf{m}$  denotes the magnetization vector, it is expected that the unconventional DL torque of  $\mathbf{x}$ -polarization and  $\mathbf{z}$ -polarization generated by MSHE will take the forms of  $\mathbf{m} \times (\mathbf{m} \times \mathbf{x})$  and  $\mathbf{m} \times (\mathbf{m} \times \mathbf{z})$ , respectively. This means that MSHE-induced SOT can be investigated quantitatively under the condition of ferromagnetic resonance. In doing so, we hope to contribute to a deeper understanding of unconventional SOT induced by MSHE<sup>20</sup>.

The non-collinear AFM L1<sub>2</sub> Mn<sub>3</sub>Pt that we focus on this paper is an antiferromagnetic material with a topologically nontrivial spin structure<sup>4,21</sup>. The crystal structure of Mn<sub>3</sub>Pt is L1<sub>2</sub> (space group:  $Pm\bar{3}m$ ), and the Néel temperature is around 475K. At room temperature, Mn<sub>3</sub>Pt has a 120° triangular  $\Gamma_{4g}$  spin structure lying in a (111) kagome plane where the spin configuration is all-in or all-out, which is similar to Mn<sub>3</sub>Ir (see Fig. 1(a))<sup>22</sup>. Mn<sub>3</sub>Pt has so far been experimentally demonstrated to exhibit a relatively large AHE<sup>23</sup> and spin Hall angle<sup>7</sup>. In addition, an intermetallic compound with the same  $\Gamma_{4g}$  spin structure also shows facet-dependence of spin Hall conductivity<sup>8</sup> and out-of-plane ( $\mathbf{z}$  direction) spin accumulation<sup>24</sup>. In this work, we use a spin-torque ferromagnetic resonance (ST-FMR) technique to explore the unconventional SOT in an L1<sub>2</sub>-ordered epitaxial Mn<sub>3</sub>Pt / Ni<sub>80</sub>Fe<sub>20</sub> (Py) heterostructure. We observed the NO-

<sup>a)</sup>Electronic mail: yu.longjie.t7dc.tohoku.ac.jp

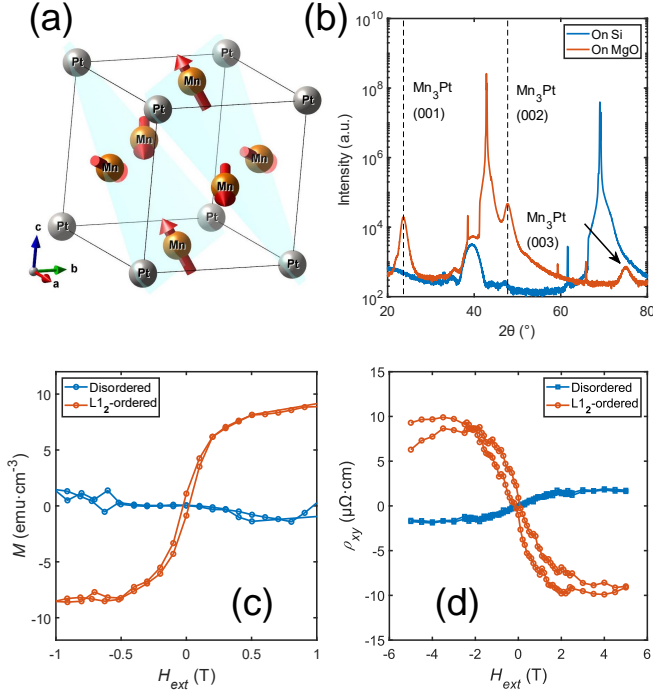


FIG. 1. (a) Crystal and magnetic structure of L<sub>12</sub>-ordered Mn<sub>3</sub>Pt. Note that the Mn atoms in the unit cell of Mn<sub>3</sub>Pt construct a kagome lattice in the (111) plane, where the spin structure is triangular and the direction of spins is either all-in or all-out. (b) X-ray diffraction patterns measured for the 15 nm-thick Mn<sub>3</sub>Pt deposited on MgO and Si substrates. (c) Measured magnetic hysteresis curves for the Mn<sub>3</sub>Pt with and without L<sub>12</sub>-ordered structure. A weak magnetization can only be detected for L<sub>12</sub>-ordered Mn<sub>3</sub>Pt. (d) AHE of samples in (c).

y spin-polarization-induced SOT in L<sub>12</sub>-ordered Mn<sub>3</sub>Pt, which is absent in poly-Mn<sub>3</sub>Pt whose lattice structure as well as spin structure are regarded as disordered. Such an SOT can be associated with the contribution from the MSHE and the configuration of AFM domains.

Mn<sub>3</sub>Pt thin films with the thickness of 15nm were grown by magnetron sputtering on a MgO (001) and a thermally oxidized Si substrate with the substrate temperature  $T_s$  of 450°C and RT, respectively. Subsequently, a thin layer of MgAl<sub>2</sub>O<sub>4</sub> (2.5 nm) was deposited at RT to prevent oxidation. The out-of-plane X-ray diffraction patterns for Mn<sub>3</sub>Pt fabricated on the MgO and Si substrates are shown in Fig. 1(b). (001) and (003) superlattice peaks originating from the L<sub>12</sub> structure could be observed clearly only for the Mn<sub>3</sub>Pt deposited on MgO, while they disappeared for the one deposited on Si. Such a result indicates that only Mn<sub>3</sub>Pt deposited on MgO forms a well-ordered L<sub>12</sub> structure, while the lattice structure of Mn<sub>3</sub>Pt deposited on Si is disordered. Therefore, we set Mn<sub>3</sub>Pt deposited on Si substrate as a control sample. In addition, we also note that the aforementioned  $\Gamma_{4g}$  spin structure only exists in the L<sub>12</sub> struc-

ture.

Next, to determine whether L<sub>12</sub> Mn<sub>3</sub>Pt had a triangular spin structure, we characterized the magnetic and magneto-transport properties with magnetic hysteresis curves and performed Hall measurement for the Mn<sub>3</sub>Pt single film in an out-of-plane applied field. To examine the magnetic properties, we compared the hysteresis curves of L<sub>12</sub>-ordered Mn<sub>3</sub>Pt and disordered Mn<sub>3</sub>Pt at 300K, as shown in Fig. 1(c). A weak but nonzero net magnetization  $M$  (about 9 emu·cm<sup>-3</sup>) was detected along the (001) direction of the L<sub>12</sub> Mn<sub>3</sub>Pt film due to triangle spin canting, which is consistent with previous theoretical<sup>4</sup> and experimental works<sup>23</sup>. The magnitude of  $M$  we measured is also similar to that for L<sub>12</sub>-ordered Mn<sub>3</sub>Ir<sup>26</sup>. In contrast, such a small magnetization could not be observed for the disordered control sample. For transport properties, we patterned the films by photolithography and ion-beam etching into a Hall bar with the channel width of 10 μm and measured transverse resistivity  $\rho_{xy}$  by applying current along [100] direction. Figure 1(d) shows  $\rho_{xy}$  as a function of the external field at 300K. Negative Hall-resistance loops were observed for L<sub>12</sub>-ordered Mn<sub>3</sub>Pt, which means the signature of AHE exists in L<sub>12</sub>-ordered Mn<sub>3</sub>Pt and corresponds to the previous observation in the Mn<sub>3</sub>X (X = Sn, Ge, Ga, Ir, Pt) family of AFM materials<sup>23,25–28</sup>.

We next evaluated the symmetry of SOT and examined the SOT components quantitatively using an ST-FMR technique<sup>16,19,20,29</sup>. The stack structures we measured were Si or MgO / Mn<sub>3</sub>Pt (15 nm) / Py (8 nm) / MgAl<sub>2</sub>O<sub>4</sub> (2.5 nm). Figure 2(a) shows the schematic geometry of the ST-FMR measurement. A microwave current  $I$  was applied to Mn<sub>3</sub>Pt, torques were generated therefore exerted to the Py. An in-plane external field was simultaneously swept at an angle  $\phi_H$  relative to  $I$ , after which a mix voltage  $V_{mix}$  modulated by the anisotropic magnetoresistance (AMR) of Py could be detected by a lock-in amplifier. Such a  $V_{mix}$  can be fitted as  $V_{mix} = V_s F_s + V_a F_a$ , where  $F_s$  and  $F_a$  denote the symmetric and antisymmetric Lorentzian functions, and  $V_s$  and  $V_a$  denote the amplitudes of  $F_s$  and  $F_a$ , respectively. Figure 2(b) shows the ST-FMR spectra of L<sub>12</sub>-ordered Mn<sub>3</sub>Pt / Py and disordered Mn<sub>3</sub>Pt / Py at 9 GHz with  $\phi_H = 40^\circ$  and symmetric and antisymmetric components separated by fitting to  $V_{mix} = V_s F_s + V_a F_a$ . The data points were fitted well by the equation above. In order to evaluate the possible DL torque and FL torque generated by NO-y polarization due to MSHE, we also performed angle-dependent ST-FMR measurements with respect to  $\phi_H$ , which a reliable approach for identifying unconventional torques. According to the symmetric analysis of spin polarization-induced SOTs that exert to the Py layer, the in-plane torque  $\tau_{\parallel}$  and out-of-plane torque  $\tau_{\perp}$  components of SOT are proportional to  $V_s$  and

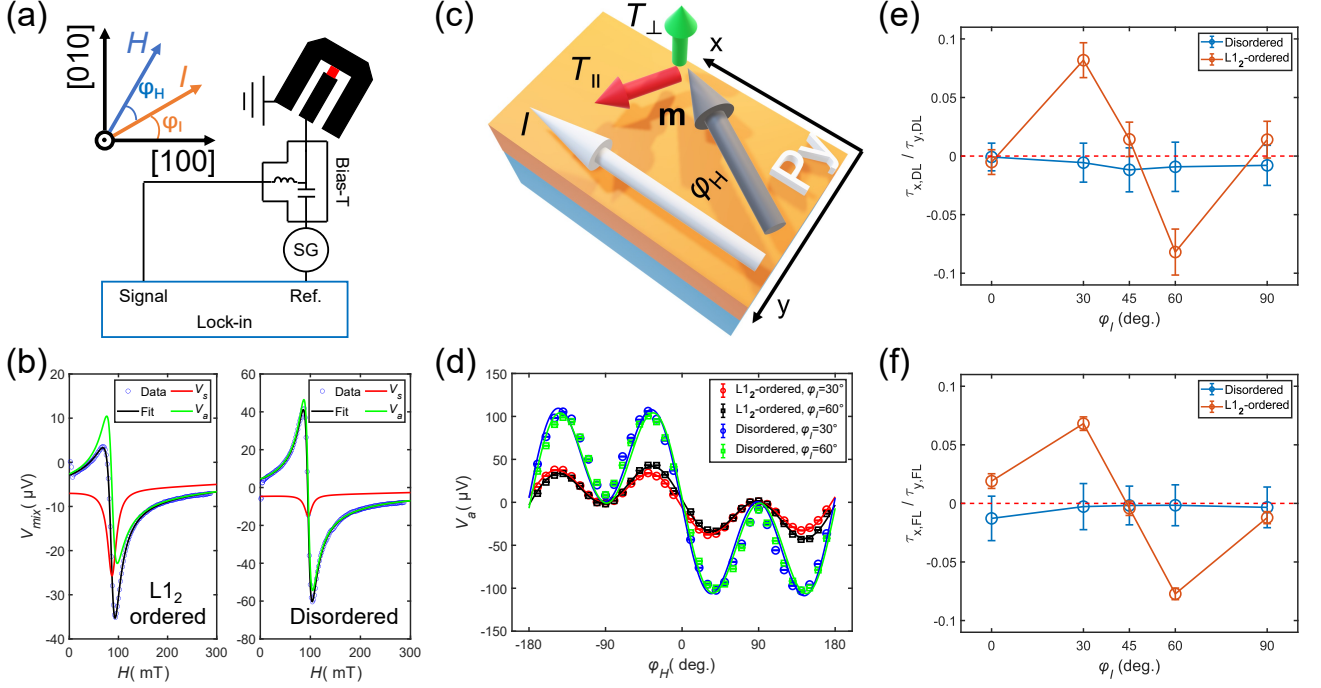


FIG. 2. (a) Schematic illustration of ST-FMR measurement. Coordinate is defined with respect to the lattice of  $\text{Mn}_3\text{Pt}$ . The red strip represents  $\text{Mn}_3\text{Pt} / \text{Py}$  bilayer. (b) Measured  $V_{mix}$  for  $\text{L}_{12}$ -ordered  $\text{Mn}_3\text{Pt} / \text{Py}$  and disordered  $\text{Mn}_3\text{Pt} / \text{Py}$  at 9 GHz with  $\phi_H = 40^\circ$ . The applied microwave power is 6 dBm. (c) Schematic of the sample geometry and SOTs acting on Py:  $\tau_{\parallel}$  is composed of  $\tau_{x,DL}$  and  $\tau_{y,DL}$ , while  $\tau_{\perp}$  is composed of  $\tau_{x,FL}$  and  $\tau_{y,FL}$ . (d) Antisymmetric ST-FMR component ( $V_a$ ) of  $\text{L}_{12}$ -ordered  $\text{Mn}_3\text{Pt} / \text{Py}$  and disordered  $\text{Mn}_3\text{Pt} / \text{Py}$  with different  $\phi_I$  as a function of  $\phi_H$ . The error bars represent fitting standard deviations. (e, f) Torque ratios  $\tau_{x,DL}/\tau_{y,DL}$  and  $\tau_{x,FL}/\tau_{y,FL}$  for  $\text{L}_{12}$ -ordered  $\text{Mn}_3\text{Pt} / \text{Py}$  and disordered  $\text{Mn}_3\text{Pt} / \text{Py}$  as a function of  $\phi_I$ .

$V_a$ , which can be expressed as<sup>19,20</sup>

$$\begin{aligned} V_s(\phi_H) &\propto \sin(2\phi_H)\tau_{\parallel} \\ &= \sin(2\phi_H)[\tau_{x,DL}\sin(\phi_H) + \tau_{y,DL}\cos(\phi_H) \\ &\quad + \tau_{z,FL}], \end{aligned} \quad (1)$$

$$\begin{aligned} V_a(\phi_H) &\propto \sin(2\phi_H)\tau_{\perp} \\ &= \sin(2\phi_H)[\tau_{x,FL}\sin(\phi_H) + \tau_{y,FL}\cos(\phi_H) \\ &\quad + \tau_{z,DL}], \end{aligned} \quad (2)$$

where  $\tau_{x,DL}$ ,  $\tau_{x,FL}$ ,  $\tau_{y,DL}$ ,  $\tau_{y,FL}$ ,  $\tau_{z,DL}$ ,  $\tau_{z,FL}$  are the DL / FL torques generated by spin currents that are polarized along the  $\mathbf{x}$ ,  $\mathbf{y}$ ,  $\mathbf{z}$  directions, respectively. Note that effects such as Rashba-like and Dresselhaus-like fields and exchange coupling at the FM and AFM interface may contribute to the above torques, as discussed below. Figure. 2(c) depicts the components of SOTs exerting on Py.

We further investigated the unconventional torques ( $\tau_x$  and  $\tau_z$ ) by patterning a series of microstrips on the same sample with different  $\phi_I$ , where  $\phi_I$  is defined as the angle between  $[100]$  orientation and  $I$ , thereby measuring the  $\phi_H$  dependence of  $V_a$  and  $V_s$ . In Fig. 2(d), we compare the  $V_a$  dependence of  $\phi_H$  for  $\text{L}_{12}$ -ordered  $\text{Mn}_3\text{Pt}$  and disordered  $\text{Mn}_3\text{Pt}$  with different  $\phi_I$ . Two phenomena could

be observed clearly for  $\text{Mn}_3\text{Pt}$  deposited on  $\text{MgO}$ , which is  $\text{L}_{12}$ -ordered: (1) there were  $\sin(2\phi_H)$  components induced by  $\tau_{x,FL}$  in the two microstrips, giving rise to the broken centrosymmetry of  $V_a$ , and (2) on the one side of plus  $\phi_H$  or minus  $\phi_H$ , the relative magnitudes of two peaks looks difficult, and the symmetry were reversed from  $\phi_I = 30^\circ$  to  $\phi_I = 60^\circ$  due to the sign reversal of  $\tau_{x,FL}$ . For instance, when  $\phi_H$  decreasing from  $-180^\circ$  to  $0^\circ$ , peak values decreased from  $37.4 \mu\text{A}$  to  $33.3 \mu\text{A}$  for  $\phi_I = 30^\circ$ , while peak values increased from  $32.7 \mu\text{A}$  to  $41.9 \mu\text{A}$  for  $\phi_I = 60^\circ$ . In contrast, these two phenomena could not be found for disordered  $\text{Mn}_3\text{Pt}$ . It is also worthwhile to note that although the magnitude of the  $V_a$  of  $\text{L}_{12}$ -ordered  $\text{Mn}_3\text{Pt}$  and disordered  $\text{Mn}_3\text{Pt}$  are obviously different due to the distinct impedance mismatch, it makes no difference to the symmetry, as discussed above.  $V_s$  also exhibited a similar behavior attribute to the existence of the  $\sin(2\phi_H)$  contribution induced by  $\tau_{x,DL}$  although not shown here. Such a result demonstrates a strong correlation between unconventional torques and the triangular spin structure. We therefore measured the  $V_a$  and  $V_s$  as a function of  $\phi_H$  from  $\phi_I = 0^\circ$  to  $\phi_I = 90^\circ$  and fitted them to Eq.(1, 2), thereby extracting the associated fitting parameters  $\tau_{x,DL}$ ,  $\tau_{x,FL}$ ,  $\tau_{y,FL}$  and plotting the ratios of  $\tau_{x,DL}/\tau_{y,DL}$  and  $\tau_{x,FL}/\tau_{y,FL}$  as a function of  $\phi_I$ , as shown in Fig. 2(e) and (f). Such

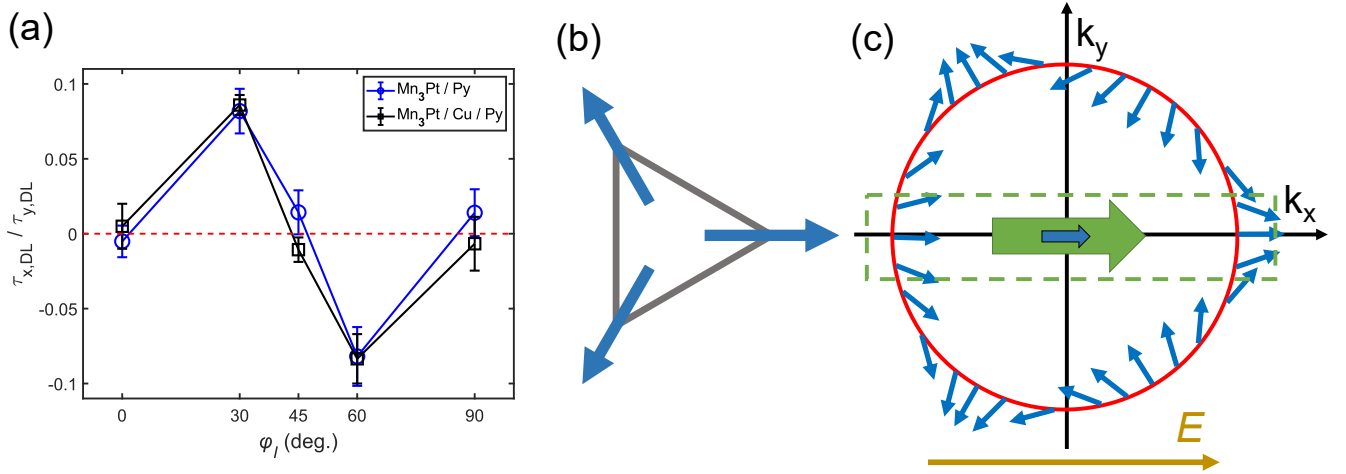


FIG. 3. (a) Comparison of  $\tau_{x,DL}/\tau_{y,DL}$  dependence of  $\phi_I$  for  $L1_2$ -ordered  $\text{Mn}_3\text{Pt}$  with or without Cu interlayer. (b)  $\Gamma_{4g}$  magnetic configuration of the  $L1_2$ -ordered  $\text{Mn}_3\text{Pt}$  possesses, and (c) its corresponding spin structure in momentum space. In the picture of MSHE<sup>18</sup>, a longitudinal spin current will be generated as a result of the non-collinear spin structure breaking the spin conservation.

a torque ratio can help us to quantitatively estimate the  $x$  component and  $y$  component that contribute to  $V_s$  and  $V_a$ . The FL torque generated by  $y$ -polarization is negligible so that Oersted field contributes  $\tau_{y,FL}$  mainly. Detectable  $\tau_{x,DL}/\tau_{y,DL}$  of about 0.08 and  $\tau_{x,FL}/\tau_{y,FL}$  of about 0.07 were observed for  $L1_2$ -ordered  $\text{Mn}_3\text{Pt}$ , and a sign inversion behavior was clearly exhibited for both ratios, which may have originated from the generation and polarization reversal of spin polarization along the  $x$  direction (current direction). However, both the detectable  $\tau_x$  and the sign inversion behavior vanish for the disordered one. Notably, compared to the conventional  $\tau_y$ , which yields a Rashba-like field with the same Rashba-like symmetry, the unconventional FL and DL torques  $\tau_{x,FL}$  and  $\tau_{x,DL}$  that have been observed above correspond to a Dresselhaus-like symmetry<sup>17,30</sup>.

The same angular-dependent experiment was carried out in  $\text{MgO} / \text{Mn}_3\text{Pt}$  (15 nm) /  $\text{Cu}$  (2 nm) /  $\text{Py}$  (8 nm) stacks with a Cu insertion layer to rule out possible effects caused by interlayer exchange coupling. We compared torque ratios  $\tau_{x,DL}/\tau_{y,DL}$  for sample with and without a Cu layer, as shown in Fig. 3(a). Remarkably, the variation as well as the values of  $\tau_{x,DL}/\tau_{y,DL}$  for the samples with a Cu spacer were quite similar to its counterpart without Cu, indicating that the interlayer effects between  $L1_2$ -ordered  $\text{Mn}_3\text{Pt}$  and  $\text{Py}$  are not likely to account for the appearance of  $x$ -polarization. The appearance of  $x$ -polarization in our  $\text{Mn}_3\text{Pt}$  sample with a triangular  $\Gamma_{4g}$  spin structure can be interpreted phenomenologically by the fact that spin-momentum locking yields MSHE<sup>15,18</sup>. Recent reports have demonstrated that the momentum space of non-collinear AFM is related strongly to its spin structure. Figure. 3(b, c) show the schematics of the triangular  $\Gamma_{4g}$  magnetic configuration in real space and the corresponding spin structure in

momentum space, respectively. Upon applying an electric field, the distribution of the electrons at the Fermi level will change, and a spin current with  $x$ -polarization along the  $x$  direction will be generated for both states of  $k_y > 0$  and  $k_y < 0$ . The property of the canted kagome plane in our (001)-oriented  $L1_2$   $\text{Mn}_3\text{Pt}$  sample will give rise to the detection of  $x$ -polarization-induced  $\tau_{x,DL}$  and  $\tau_{x,FL}$ , since the canted kagome plane makes the spin current no longer parallel to the  $x$ -direction, which is consistent with the experimental results. In addition, the theoretical calculation of spin Hall conductivity for the  $\Gamma_{4g}$  magnetic configuration performed in previous works also predicted the existence of  $x$ -polarization<sup>18,24</sup>. Although the mechanism underlying the sign reversal behavior and the symmetry related to  $\phi_I = 45^\circ$  for both torque ratios  $\tau_{x,DL}/\tau_{y,DL}$  and  $\tau_{x,FL}/\tau_{y,FL}$  in Fig. 2(e), (f) remain unknown, we presume that one possible factor is the contribution from the AFM domain configuration. In fact, an AFM domain configuration that modulates the SOT efficiency in the collinear AFM  $\text{IrMn} / \text{Py}$  bilayer was recently reported<sup>9</sup>, which highlights the correlation between AFM domain configuration and SOT. It is worthwhile noting that the  $x$ -polarization generated by spin-momentum locking also to be facet-dependent, as the triangular magnetic momentum points to a different crystalline orientation. These contributions from facet-dependent spin momentum locking and AFM domain configuration are extremely likely to give rise to the sign reversal behavior. Further research should be undertaken to investigate the correlation between non-collinear AFM domain configuration and the symmetry of the unconventional SOT to supplement what is reported above.

In this paper, we have demonstrated the generation of an unconventional SOT (mainly  $x$ -direction) in

non-collinear AFM L<sub>12</sub>-ordered Mn<sub>3</sub>Pt with a topologically nontrivial spin structure. This unconventional  $\mathbf{x}$ -polarization in the SOT exhibited a unique symmetry with respect to the applied current direction, while both the unconventional SOT and the concomitant unique symmetry vanished in disordered Mn<sub>3</sub>Pt. Invariance of the sample with a Cu spacer excluded the possible effects from interlayer coupling, suggesting that the observation of unconventional SOT can be attributed to the MSHE and AFM domain configuration in L<sub>12</sub>-ordered Mn<sub>3</sub>Pt. Our findings provide the insight into how unconventional SOT can be generated by taking advantage of the topological spin structure in non-collinear AFM. In addition, this work offers new perspectives to clarify the underlying physics for charge to spin conversions in non-collinear AFMs.

This work was partially supported by the Center for Science and Innovation in Spintronics (CSIS), the Center for Spintronics Research Network (CSRN), and the GP-Spin program at Tohoku University.

- <sup>1</sup>V. Baltz, A. Manchon, M. Tsoi, T. Moriyama, T. Ono, and Y. Tserkovnyak, *Rev. Mod. Phys.* **90**, 015005 (2018).
- <sup>2</sup>M. B. Jungfleisch, W. Zhang, and A. Hoffmann, *Phys. Lett. A* **382**, 865 (2018).
- <sup>3</sup>L. Šmejkal, Y. Mokrousov, B. Yan, and A. H. MacDonald, *Nat. Phys.* **14**, 242 (2018).
- <sup>4</sup>H. Chen, Q. Niu, and A. H. MacDonald, *Phys. Rev. Lett.* **112**, 017205 (2014).
- <sup>5</sup>S. Nakatsuji, N. Kiyohara, and T. Higo, *Nature* **527**, 212 (2015).
- <sup>6</sup>A. Fert, N. Reyren, and V. Cros, *Nat. Rev. Mater.* **2**, 1 (2017).
- <sup>7</sup>W. Zhang, M. B. Jungfleisch, W. Jiang, J. E. Pearson, A. Hoffmann, F. Freimuth, and Y. Mokrousov, *Phys. Rev. Lett.* **113**, 196602 (2014).
- <sup>8</sup>W. Zhang, W. Han, S.-H. Yang, Y. Sun, Y. Zhang, B. Yan, and S. S. Parkin, *Sci. Adv.* **2**, e1600759 (2016).
- <sup>9</sup>J. Zhou, X. Wang, Y. Liu, J. Yu, H. Fu, L. Liu, S. Chen, J. Deng, W. Lin, X. Shu, *et al.*, *Sci. Adv.* **5**, eaau6696 (2019).
- <sup>10</sup>P. Wadley, B. Howells, J. Železný, C. Andrews, V. Hills, R. P. Campion, V. Novák, K. Olejník, F. Maccherozzi, S. Dhesi, *et al.*, *Science* **351**, 587 (2016).
- <sup>11</sup>X. Chen, X. Zhou, R. Cheng, C. Song, J. Zhang, Y. Wu, Y. Ba, H. Li, Y. Sun, Y. You, *et al.*, *Nat. Mater.* **18**, 931 (2019).
- <sup>12</sup>Y. Takeuchi, Y. Yamane, J.-Y. Yoon, R. Itoh, B. Jinnai, S. Kanai, J. Ieda, S. Fukami, and H. Ohno, *Nat. Mater.* , 1 (2021).
- <sup>13</sup>M. Kimata, H. Chen, K. Kondou, S. Sugimoto, P. K. Muduli, M. Ikhlas, Y. Omori, T. Tomita, A. H. MacDonald, S. Nakatsuji, *et al.*, *Nature* **565**, 627 (2019).
- <sup>14</sup>J. Holanda, H. Saglam, V. Karakas, Z. Zang, Y. Li, R. Divan, Y. Liu, O. Ozatay, V. Novosad, J. E. Pearson, *et al.*, *Phys. Rev. Lett.* **124**, 087204 (2020).
- <sup>15</sup>A. Mook, R. R. Neumann, A. Johansson, J. Henk, and I. Mertig, *Phys. Rev. Research* **2**, 023065 (2020).
- <sup>16</sup>X. Chen, S. Shi, G. Shi, X. Fan, C. Song, X. Zhou, H. Bai, L. Liao, Y. Zhou, H. Zhang, *et al.*, *Nat. Mater.* **20**, 800 (2021).
- <sup>17</sup>H. Kurebayashi, J. Sinova, D. Fang, A. Irvine, T. Skinner, J. Wunderlich, V. Novák, R. Campion, B. Gallagher, E. Vehstedt, *et al.*, *Nat. Nanotechnol.* **9**, 211 (2014).
- <sup>18</sup>J. Železný, Y. Zhang, C. Felser, and B. Yan, *Phys. Rev. Lett.* **119**, 187204 (2017).
- <sup>19</sup>T. Nan, C. X. Quintela, J. Irwin, G. Gurung, D.-F. Shao, J. Gibbons, N. Campbell, K. Song, S.-Y. Choi, L. Guo, *et al.*, *Nat. Commun.* **11**, 1 (2020).
- <sup>20</sup>D. MacNeill, G. Stiehl, M. Guimaraes, R. Buhrman, J. Park, and D. Ralph, *Nat. Phys.* **13**, 300 (2017).
- <sup>21</sup>E. Krén, G. Kádár, L. Pál, J. Sólyom, P. Szabó, and T. Tarnóczy, *Phys. Rev.* **171**, 574 (1968).
- <sup>22</sup>A. Kohn, A. Kovács, R. Fan, G. McIntyre, R. Ward, and J. Goff, *Sci. Rep.* **3**, 1 (2013).
- <sup>23</sup>Z. Liu, H. Chen, J. Wang, J. Liu, K. Wang, Z. Feng, H. Yan, X. Wang, C. Jiang, J. Coey, *et al.*, *Nat. Electron.* **1**, 172 (2018).
- <sup>24</sup>Y. Liu, Y. Liu, M. Chen, S. Srivastava, P. He, K. L. Teo, T. Phung, S.-H. Yang, and H. Yang, *Phys. Rev. Applied* **12**, 064046 (2019).
- <sup>25</sup>T. Ikeda, M. Tsunoda, M. Oogane, S. Oh, T. Morita, and Y. Ando, *Appl. Phys. Lett.* **113**, 222405 (2018).
- <sup>26</sup>H. Iwaki, M. Kimata, T. Ikebuchi, Y. Kobayashi, K. Oda, Y. Shiota, T. Ono, and T. Moriyama, *Appl. Phys. Lett.* **116**, 022408 (2020).
- <sup>27</sup>N. Kiyohara, T. Tomita, and S. Nakatsuji, *Phys. Rev. Applied* **5**, 064009 (2016).
- <sup>28</sup>J. Mukherjee, T. Suraj, H. Basumatary, K. Sethupathi, and K. V. Raman, *Phys. Rev. Materials* **5**, 014201 (2021).
- <sup>29</sup>L. Liu, T. Moriyama, D. Ralph, and R. Buhrman, *Phys. Rev. Lett.* **106**, 036601 (2011).
- <sup>30</sup>C. Ciccarelli, L. Anderson, V. Tshitoyan, A. Ferguson, F. Gerhard, C. Gould, L. Molenkamp, J. Gayles, J. Železný, L. Šmejkal, *et al.*, *Nat. Phys.* **12**, 855 (2016).